Self-consistent gyrokinetic modeling of neoclassical and turbulent impurity transport

D. Estève, Y. Sarazin, X. Garbet, V. Grandgirard, S. Breton, P. Donnel, Y. Asahi, C. Bourdelle, G. Dif-Pradalier, C. Ehrlacher, et al.

Self-consistent gyrokinetic modeling of neoclassical and turbulent impurity transport

D. Estève[1], Y. Sarazin[1], X. Garbet[1], V. Grandgirard[1], S. Breton[1], P. Donnel[1], Y. Asahi[1,2], C. Bourdelle[1], G. Dif-Pradalier[1], C. Ehrlacher[1], C. Emeriau[1,3], Ph. Ghendrih[1], C. Gillot[1], G. Latu[1], C. Passeron[1]

1 CEA, IRFM, F-13108 Saint-Paul-lez-Durance cedex, France.
2 Japan Atomic Energy Agency, Wakashiba 178-4, Kashiwa, Chiba 277-0871, Japan
3 Laboratoire AIM Paris-Saclay, CEA/Irfu Université Paris-Diderot CNRS/INSU, F-91191 Gif-sur-Yvette, France

E-mail: yanick.sarazin@cea.fr

13 October 2016

Abstract.

Trace impurity transport is studied with the flux-driven gyrokinetic GYSELA code [V. Grandgirard et al., *Comp. Phys. Commun.* **207**, 35 (2016)]. A reduced and linearized multi-species collision operator has been recently implemented, so that both neoclassical and turbulent transport channels can be treated self-consistently on an equal footing. In the Pfirsch-Schlüter regime likely relevant for tungsten, the standard expression of the neoclassical impurity flux is shown to be recovered from gyrokinetics with the employed collision operator. Purely neoclassical simulations of deuterium plasma with trace impurities of helium, carbon and tungsten lead to impurity diffusion coefficients, inward pinch velocities due to density peaking, and thermo-diffusion terms which quantitatively agree with neoclassical predictions and NEO simulations [E. Belli et al., *Plasma Phys. Control. Fusion* **54**, 015015 (2012)]. The thermal screening factor appears to be less than predicted analytically in the Pfirsch-Schlüter regime, which can be detrimental to fusion performance. Finally, self-consistent nonlinear simulations have revealed that the tungsten impurity flux is not the sum of turbulent and neoclassical fluxes computed separately, as usually assumed. The synergy mostly results from the turbulence-driven in-out poloidal asymmetry of tungsten density. This result puts forward the need for self-consistent simulations of impurity transport, i.e. including both turbulence and neoclassical physics, in view of quantitative predictions for ITER.

1. Introduction

Impurity transport studies have recently gained a renewed interest with the perspective of using tungsten divertors in ITER [1] and WEST [2, 3] tokamaks. High-Z materials such as tungsten ($Z_W = 74$) are only partially ionized even in the plasma core despite high temperatures, so that they can already lead to prohibitive radiative losses at low

concentrations [4]. These losses then impact dramatically plasma performance and stability. Actually, on-axis accumulation of tungsten has been reported in several tokamaks, including H-mode plasmas in JET [5] and ASDEX Upgrade [6]. Conversely, in Alcator-Cmod, relatively flat electron density profiles combined with peaked electron temperature in the central region appear to be efficient to prevent tungsten accumulation in the core [7]. Tungsten is not the only impurity to be present in ITER plasmas. In addition to helium ashes, extrinsic impurities will also be present, due to medium-Z (such as neon $Z_{Ne} = 10$ and argon $Z_{Ar} = 18$) impurity seeding aiming at radiating the power at the edge, and low-Z beryllium ($Z_{Be} = 4$) due to plasma wall interactions.

Impurity transport is actually a complex issue, even in the relevant limit of trace impurities where their strength parameter is negligible ($\alpha = n_Z Z^2/n_i Z_i^2 \ll 1$, with Z the impurity and i the main ion species). The radial impurity flux contains both a diffusive and a convective contribution: $\Gamma_Z = -D\nabla n_Z + V n_Z$. In the absence of transport barriers, in L-mode plasmas, impurity transport is usually found to be dominated by turbulence, at least in the gradient region. Indeed, the experimentally deduced transport coefficients exceed the ones predicted by the neoclassical theory by factors or even orders of magnitudes in tokamak plasmas [8, 9, 10, 11] and spherical tokamaks [12, 13]. Conversely, in the very core region [14, 15, 16] and at the position of transport barriers, either at the edge or at internal transport barriers, impurity transport is often found consistent with neoclassical predictions [17, 18, 19]. In such regimes, the impurity confinement time sometimes appears to scale with the edge density gradient of the main ion species, as one would expect from neoclassical transport theory [20]. Should neoclassical transport dominate tungsten transport in ITER H-mode edge plasmas, tungsten is then expected to exhibit hollow density profiles in the pedestal region [21].

In addition, it has been recently realized that standard neoclassical predictions for impurity transport can be substantially modified in the highly collisional regime (Pfirsch-Schlüter), relevant for high-Z impurities, in the case where their density profile exhibits in-out asymmetry [22, 23, 24, 25]. Such poloidal asymmetries can emerge as a result of centrifugal force [26] or of anisotropic (i.e. such that $T_\perp \neq T_\parallel$) radio-frequency heating, especially Ion Cyclotron Resonance Heating [27, 28, 29].

All in all, it appears that the turbulent and neoclassical coefficients for impurity transport, both diffusivity and convection velocity, can be of the same order of magnitude, especially for high-Z impurities such as tungsten. At present, first principles simulations of these transports are performed with different dedicated codes, explicitly assuming that both transport channels are additive (see e.g. [7]). One of the key questions is whether this assumption is valid, or whether neoclassical and turbulent transports exhibit synergetic effects which would modify our understanding and predictions of impurity concentration in tokamaks.

In this framework, a multi-species collision operator has been developed for full-f gyrokinetic codes and successfully implemented [30] in the flux-driven GYSELA code [31]. In this paper, we first show analytically that this operator allows one to

recover neoclassical predictions of impurity transport in the Pfirsch-Schlüter regime (section 2). The numerical benchmark of the code with respect to neoclassical theory for trace impurity transport is then successfully performed in section 3 in all three regimes of collisionality (banana, plateau and Pfirsch-Schlüter) by considering different types of impurities. Last but not least, section 4 presents the first evidence of synergy between turbulent and neoclassical transport of tungsten. Turbulence driven poloidal asymmetries are suspected to play a key role in this synergy.

2. Recovering neoclassical fluxes from gyrokinetics

2.1. Radial flux and toroidal momentum conservation

The spatial coordinates are (ψ, θ, φ) where ψ is the minus poloidal magnetic flux normalized to 2π, θ is the poloidal angle and φ the toroidal angle. The Jacobian of this metric is $1/\mathbf{B}\cdot\nabla\theta$ where the unperturbed magnetic field is

$$\mathbf{B} = I\nabla\varphi + \nabla\varphi\times\nabla\psi \tag{1}$$

We consider the gyrocenter distribution function $F(\mathbf{z})$ where $\mathbf{z} = (\psi, \theta, \varphi, v_\parallel, \mu)$ are the gyrocenter coordinates. Here $v_\parallel$ is the gyrocenter parallel velocity and μ the magnetic moment. To derive the conservation laws, it is convenient to use the gyrokinetic Fokker-Planck equation [32, 33]

$$\frac{\partial F}{\partial t} + \frac{1}{B^*_{||}}\frac{\partial}{\partial \mathbf{z}}\cdot\left(\dot{\mathbf{z}}B^*_{||}F\right) = C(F) \tag{2}$$

where $\dot{\mathbf{z}} = \frac{d\mathbf{z}}{dt}$ and

$$B^*_{||} = B + \frac{mv_\parallel}{e}\mathbf{b}\cdot(\nabla\times\mathbf{b}) \tag{3}$$

is the Jacobian of the gyrocenter transformation (m is the mass, e the charge and $\mathbf{b} = \frac{\mathbf{B}}{B}$ the unit vector along the magnetic field). For an electrostatic case, the gyrocenter equations of motion are

$$B^*_{||}\frac{d\mathbf{x}}{dt} = -B^*_{||}[H, \mathbf{x}] = v_\parallel\mathbf{B}^* + \frac{1}{e}\mathbf{b}\times\nabla\left(\mu B + e\bar{\phi}\right) \tag{4}$$

$$B^*_{||}m\frac{dv_\parallel}{dt} = -B^*_{||}[H, mv_\parallel] = -\mathbf{B}^*\cdot\nabla\left(\mu B + e\bar{\phi}\right) \tag{5}$$

where

$$\mathbf{B}^* = \mathbf{B} + \frac{mv_\parallel}{e}\nabla\times\mathbf{b} \tag{6}$$

and

$$H = \frac{1}{2}mv_\parallel^2 + \mu B + e\bar{\phi} \tag{7}$$

is the Hamiltonian, $\bar{\phi} = J\cdot\phi$ are the gyro-average electric potential. It was shown by several authors [34, 35, 36, 37] that the toroidal momentum conservation equation reads

$$\partial_t\mathcal{L}_\varphi + \partial_\psi\Pi^\psi_\varphi = e\left(\Gamma^\psi - \Gamma^\psi_E\right) + \left\langle\frac{I}{B}R_\parallel\right\rangle_\psi \tag{8}$$

where

$$\mathcal{L}_\varphi = m \int d\tau u_\varphi F \tag{9}$$

$$\Pi_\varphi^\psi = m \int d\tau F u_\varphi v^\psi \tag{10}$$

$$\Gamma_E^\psi = \int d\tau F \partial_\varphi \bar{\phi} \tag{11}$$

$$\Gamma^\psi = \int d\tau v^\psi F = \langle \mathbf{\Gamma}_\perp \cdot \nabla\psi \rangle_\psi \tag{12}$$

where $R_\parallel$ is the collisional drag force

$$R_\parallel = \int d^3\mathbf{v} m v_\parallel C(F) \tag{13}$$

with $d^3\mathbf{v} = \frac{2\pi}{m} B_\parallel^* d\mu dv_\parallel$. $\mathbf{\Gamma}_\perp$ is the perpendicular flux. Here $u_\varphi = \frac{I}{B} v_\parallel$ is the toroidal covariant component of the gyrocenter velocity (dimensionally: $[u_\varphi] = L^2.T^{-1}$), while $v^\psi = \mathbf{v}_G \cdot \nabla\psi$ is the radial projection (or the radial contra-variant component) of the gyrocenter velocity $\mathbf{v}_G$. The phase space volume element in between two magnetic surfaces ψ and $\psi + d\psi$ is

$$d\tau = d^3\mathbf{v} \, \frac{d\theta d\varphi}{\mathbf{B} \cdot \nabla\theta} \tag{14}$$

The bracket $\langle ... \rangle_\psi$ indicates a flux surface average

$$\langle ... \rangle_\psi = \frac{\int \frac{d\theta d\varphi}{\mathbf{B}\cdot\nabla\theta} ...}{\int \frac{d\theta d\varphi}{\mathbf{B}\cdot\nabla\theta}} \tag{15}$$

The collision friction force (last term in the r.h.s. of Eq.(8)) did not appear in earlier derivations of the momentum conservation equation, either because the collisionless problem was treated, or because an unique species was considered. It is however easy to add. The flux Γ_E^ψ is the radial flux due to the $E \times B$ drift velocity. The sum over all species is a polarization flux, which can be neglected for now. The divergence of the Reynolds stress $\partial_\psi \Pi_\varphi^\psi$ contains a turbulent contribution, which is expected to be ρ_* smaller than the flux in the gyrokinetic ordering $k_\parallel R \simeq o(\rho_*)$. The neoclassical contribution to Π_φ^ψ is predicted to be even smaller. In steady-state, the flux average of Eq.(8) then gives

$$\Gamma^\psi = \Gamma_E^\psi + \Gamma_{coll}^\psi \tag{16}$$

$$\Gamma_{coll}^\psi = -\frac{I}{e} \left\langle \frac{R_\parallel}{B} \right\rangle_\psi \tag{17}$$

This equation is often recast as

$$\Gamma_{coll}^\psi = \Gamma_{BP}^\psi + \Gamma_{PS}^\psi \tag{18}$$

where

$$\Gamma_{PS}^\psi = -\frac{I}{e} \left\langle R_\parallel \left(\frac{1}{B} - \frac{B}{\langle B^2 \rangle_\psi} \right) \right\rangle_\psi \tag{19}$$

and

$$\Gamma_{BP}^{\psi} = -\frac{I}{e}\frac{\left\langle R_{\parallel} B \right\rangle_{\psi}}{\left\langle B^2 \right\rangle_{\psi}} \tag{20}$$

are respectively the Pfirsch-Schlüter and Banana-Plateau fluxes. This splitting anticipates the fact that, in the Pfirsch-Schlüter regime, the collisional drag force $R_{\parallel}$ is governed by the compressibility of both parallel velocity and parallel heat flux (cf. eqs.(35),(37)) due to the inhomogeneity of the magnetic field. In absence of turbulence, the flux Γ_E^{ψ} due to the $E \times B$ drift velocity is small since the poloidal asymmetries of the electric potential are small. The flux Γ_{coll}^{ψ} then coincides with the conventional definition of the neoclassical flux.

2.2. Collision operator

We address now the multi-species case. The collision operator for a species "a" that is implemented in the GYSELA code [31] is a simplified one [30], namely $C_a\left(F_a\right) = \sum_b C_{ab}\left(F_a\right)$ where the contribution from collisions species "a" colliding with species "b" is

$$\begin{aligned} C_{ab}\left(F_a\right) = & \frac{1}{B_{\parallel}^*}\frac{\partial}{\partial v_{\parallel}}\left[B_{\parallel}^* D_{d,ab} F_{M0a}\frac{\partial}{\partial v_{\parallel}}\left(f_a - \frac{m_a v_{\parallel} U_{\parallel d,a}}{T_a}\right)\right] \\ & - \nu_{s,ab}\frac{m_a v_{\parallel}}{T_a}\left(U_{\parallel d,a} - U_{\parallel ba}\right) F_{M0a} \\ & + \frac{2}{3}\frac{q_{ab}}{N_a T_a}\left(\frac{m_a v^2}{2T_a} - \frac{3}{2}\right) F_{M0a} \end{aligned} \tag{21}$$

where $f_a = \frac{F_a}{F_{M0a}}$. Expression of the deflection diffusion $D_{d,ab}$ and the collisional friction rate $\nu_{s,ab}$ are given in Appendix A. The distribution F_{M0a} is the unshifted Maxwellian built with the density N_a and the temperature T_a

$$F_{M0a}\left(\mathbf{x}, \mathbf{v}, t\right) = N_a\left(\mathbf{x}, t\right)\left(\frac{m_a}{2\pi T_a\left(\mathbf{x}, t\right)}\right)^{3/2} \exp\left(-\frac{E}{T_a\left(\mathbf{x}, t\right)}\right) \tag{22}$$

The single species restoring momentum coefficient is

$$\frac{m_a v}{T_a} U_{\parallel d,a}(v) = \frac{3}{4\pi}\int d\Omega \xi f_a(v, \xi, \gamma)) \tag{23}$$

where $\xi = v_{\parallel}/v$ and $d\Omega = 2\pi d\xi$ is the element of solid angle in the velocity space. The inter-species momentum restoring coefficients are

$$U_{\parallel ab} = \frac{\left\langle \nu_{s,ab} v_{\parallel} f_a \right\rangle_a}{\left\langle \nu_{s,ab}\frac{m_a v_{\parallel}^2}{T_a} \right\rangle_a} \tag{24}$$

where

$$\left\langle ... \right\rangle_a = \frac{1}{N_a}\int 2\pi \frac{B_{\parallel}^*}{B} v_{\perp} dv_{\perp} dv_{\parallel} F_{M0a} ... = \frac{2}{\sqrt{\pi}}\int_0^{\infty} dx_a x_a^2 e^{-x_a^2}\int_{-1}^{+1} d\xi ... \tag{25}$$

The energy restoring coefficient is

$$q_{ab} = N_a T_a \left\langle \sigma_{ab} f_a \right\rangle_a + Q_{ab}^M \tag{26}$$

where $Q_{ab}^M = -3N_a \frac{m_a}{m_a+m_b} \nu_{ab}(T_a - T_b)$ is the energy exchange between two centered Maxwellians and $\sigma_{ab}(v)$ is given by

$$\sigma_{ab}(v) = -\nu_{d,ab} \frac{m_a v^2}{2T_a} v_\parallel \frac{\partial}{\partial v_\parallel} \ln\left(D_{d,ab} F_{M0a} v_\parallel\right) \tag{27}$$

Standard GYSELA simulations use a limited number of mesh points in the μ space (typically 16). Therefore, so as to minimize the error when computing the friction force, the distribution function is projected on the two first Sonine polynomials (generalized Laguerre $L_j^{(m)}$ polynomials of order $m = 3/2$) in the velocity modulus space (cf. reference [36], appendix D). The friction part of the field particle collision operator (2nd line of Eq.(21)) then reads

$$\begin{aligned} C_{s,ab}\left(F_a\right) \;=\; & -\nu_{s,ab} \frac{m_a v \xi}{T_a} F_{M0a} \left\{ V_{\parallel a} - V_{\parallel b} \right. \\ & \left. + \frac{2}{5}\left(\frac{m_a v^2}{2T_a} - \frac{5}{2}\right) \frac{q_{\parallel a}}{N_a T_a} + \frac{3}{5} \frac{1}{1+x_{ba}^2} \frac{q_{\parallel b}}{N_b T_b} \right\} \end{aligned} \tag{28}$$

where $V_{\parallel a}$ and $q_{\parallel a}$ are the parallel velocity and heat flux. The friction force can then be written as

$$R_{\parallel ab} = -N_a m_a \nu_{ab} \left(V_{\parallel a} - V_{\parallel b} - \frac{3}{5} \frac{1}{1+x_{ab}^2} \frac{q_{\parallel a}}{N_a T_a} + \frac{3}{5} \frac{1}{1+x_{ba}^2} \frac{q_{\parallel b}}{N_b T_b} \right) \tag{29}$$

where $x_{ab} = \frac{v_{Tb}}{v_{Ta}}$.

2.3. Neoclassical impurity flux

We consider now the case of two ion species only: the main ion "i" and a heavy impurity "Z", which is supposed to be in a collisional (Pfirsch-Schlüter) regime. We consider here a neoclassical case, i.e. we ignore the flux due to the $E \times B$ drift velocity in Eq.(16). The impurity flux is calculated by using the relationship between the flux and the parallel collisional drag force Eq.(17)

$$\left\langle \mathbf{\Gamma}_Z \cdot \nabla \psi \right\rangle_\psi = -\frac{I}{Ze} \left\langle \frac{R_{\parallel Zi}}{B} \right\rangle_\psi \tag{30}$$

Since $x_{Zi} = v_{Ti}/v_{TZ} \gg 1$, the contribution from the parallel impurity flux in $R_{\parallel Zi}$ Eq.(29) is negligible so that

$$R_{\parallel Zi} = -N_Z m_Z \nu_{Zi} \left(V_{\parallel Z} - V_{\parallel i} + \frac{3}{5} \frac{q_{\parallel i}}{N_i T_i} \right) \tag{31}$$

In principle, the parallel flows should be calculated by solving a kinetic equation for each species. The calculation is demanding for ions in weakly collisional regime because of the

boundary layer near the transition from passing to trapped particles [42, 43, 23, 24]. The complete calculation is delicate and we give here an approximate derivation, which allows recovering the Hirshman expression of the thermal screening coefficient. For passing particles, an acceptable solution of the Fokker-Planck equation is $F_a = F_{Ma} + \delta F_a$, where δF_a is of the form

$$\delta F_a = F_{Ma} \frac{m_a v_\parallel}{T_{a,eq}} \left[W_a B - \frac{I T_{a,eq}}{e} \frac{\partial \ln F_{M0a}}{\partial \psi} \left(\frac{1}{B} - \frac{B}{\langle B^2 \rangle_\psi} \right) \right] \tag{32}$$

where

$$W_a = \frac{\langle V_{\parallel a} B \rangle_\psi}{\langle B^2 \rangle_\psi} + \frac{2}{5} \left(\frac{E}{T_{a,eq}} - \frac{5}{2} \right) \frac{1}{P_{a,eq}} \frac{\langle q_{\parallel a} B \rangle_\psi}{\langle B^2 \rangle_\psi} \tag{33}$$

and

$$T_{a,eq} \frac{\partial \ln F_{M0a}}{\partial \psi} = \left(\frac{1}{N_{a,eq}} \frac{\partial P_{a,eq}}{\partial \psi} + e_a \frac{\partial \Phi_{eq}}{\partial \psi} \right) + \left(\frac{E}{T_{eq}} - \frac{5}{2} \right) \frac{\partial T_{a,eq}}{\partial \psi} \tag{34}$$

The approximate distribution function Eq.(32) yields the following expressions of the parallel velocities and heat fluxes

$$V_{\parallel a} = \frac{\langle B V_{\parallel a} \rangle_\psi B}{\langle B^2 \rangle_\psi} - \Omega_a I \left(\frac{1}{B} - \frac{B}{\langle B^2 \rangle_\psi} \right) \tag{35}$$

where

$$\Omega_a(\psi) = \frac{1}{N_{a,eq} e_a} \frac{\partial P_{a,eq}}{\partial \psi} + \frac{\partial \Phi_{eq}}{\partial \psi} \tag{36}$$

and

$$q_{\parallel a} = \frac{\langle B q_{\parallel a} \rangle_\psi B}{\langle B^2 \rangle_\psi} - \frac{5}{2} P_{a,eq} \frac{1}{e_a} \frac{\partial T_{a,eq}}{\partial \psi} I \left(\frac{1}{B} - \frac{B}{\langle B^2 \rangle_\psi} \right) \tag{37}$$

where $N_{a,eq}$, $T_{a,eq}$ and $P_{a,eq}$ are the unperturbed density, temperature and pressure, Φ_{eq} the unperturbed electric potential. These expressions can then be plugged into Eq.(31). However one problem remains: the flux surface average of the parallel velocity and heat flux are unknown. Since heavy impurities are supposed to be in the fluid regime (i.e. such that the pressure anisotropy can be neglected: $\boldsymbol{\nabla} : \Pi \simeq \boldsymbol{\nabla} P$, with Π the pressure tensor and P the scalar pressure), the parallel force balance equation reads

$$R_{\parallel Zi} = \nabla_\parallel P_Z + N_{Z,eq} Z e \nabla_\parallel \Phi \tag{38}$$

which implies

$$\langle B R_{\parallel Zi} \rangle_\psi = 0 \tag{39}$$

and therefore

$$\langle B V_{\parallel Z} \rangle_\psi = \langle B V_{\parallel i} \rangle_\psi - \frac{3}{5} \langle B q_{\parallel i} \rangle_\psi \tag{40}$$

Hirshman et al. [42] showed that

$$\langle q_\parallel B \rangle_\psi \simeq \epsilon^{1/2} q_\parallel^* B_0 \tag{41}$$

where $q_\parallel^* = \frac{q}{\epsilon} N_{eq} T_{eq} \frac{T_{eq}}{eBL_p}$ is the parallel diamagnetic heat flux . So $\left\langle q_\parallel B \right\rangle_\psi$ can be neglected in the limit of small inverse aspect ratio $\epsilon \ll 1$. This leads to the well known constraint of equal average velocities of ions and impurities

$$\left\langle BV_{\parallel Z} \right\rangle_\psi = \left\langle BV_{\parallel i} \right\rangle_\psi \tag{42}$$

This is actually the weak point of the demonstration. The limit of large aspect ratio is indeed a poor one, and never fulfilled in actual numerical simulations. We nevertheless pursue the calculation in that framework to find an explicit expression of the friction force (accounting for the fact that $\partial_\psi \ln T_{Z,eq} \ll Z \partial_\psi \ln T_{i,eq}$ at equal temperature)

$$\begin{aligned} R_{\parallel Zi} = \nu_{Zi} \frac{m_Z T_{Z,eq}}{Ze} I \left(\frac{1}{B} - \frac{B}{\langle B^2 \rangle_\psi} \right) \\ N_{Z,eq} \left[\frac{\partial \ln N_{Z,eq}}{\partial \psi} - Z \frac{\partial \ln N_{i,eq}}{\partial \psi} + \frac{Z}{2} \frac{\partial \ln T_{i,eq}}{\partial \psi} \right] \end{aligned} \tag{43}$$

and consequently the impurity flux

$$\begin{aligned} \langle \mathbf{\Gamma}_Z \cdot \nabla \psi \rangle_\psi \; = \; - \nu_{Zi} \frac{m_Z T_{Z,eq}}{Z^2 e^2} I^2 \left(\left\langle \frac{1}{B^2} \right\rangle_\psi - \frac{1}{\langle B^2 \rangle_\psi} \right) \\ N_{Z,eq} \left(\frac{\partial \ln N_{Z,eq}}{\partial \psi} - Z \frac{\partial \ln N_{i,eq}}{\partial \psi} + \frac{Z}{2} \frac{\partial \ln T_{i,eq}}{\partial \psi} \right) \end{aligned} \tag{44}$$

In circular concentric geometry, large aspect ratio, $\frac{d\psi}{dr} = \frac{r}{q}$ and

$$I^2 \left(\left\langle \frac{1}{B^2} \right\rangle_\psi - \frac{1}{\langle B^2 \rangle_\psi} \right) \simeq 2r^2 \tag{45}$$

This formula then reads

$$\Gamma_Z^{neo} = \langle \mathbf{\Gamma}_Z \cdot \nabla r \rangle_\psi = -N_{Z,eq} \, D_z^{neo} \left\{ \frac{\partial \ln N_{Z,eq}}{\partial r} - Z_z \, \frac{\partial \ln N_{i,eq}}{\partial r} - Z_z H_z^{neo} \, \frac{\partial \ln T_{i,eq}}{\partial r} \right\} \tag{46}$$

The neoclassical diffusion coefficient is $D_z^{neo} = 2q^2 \nu_{Zi} \rho_Z^2$ in the Pfirsch-Sclüter regime, where $\nu_{iZ} = \sqrt{2} \nu_i \frac{N_{Z,eq} Z^2}{N_{i,eq}}$ and $\rho_Z = \frac{m_Z v_{TZ}}{ZeB_0}$. We recall that $N_{Z,eq} m_Z \nu_{Zi} = N_{i,eq} m_i \nu_{iZ}$. The last two terms of eq. (46) are the main off-diagonal terms of the transport matrix. The pinch velocity often refers to $V_z^{pinch} = D_z^{neo} Z_z \, \partial_r (\ln N_{i,eq})$. The thermal screening factor H_z^{neo} is expected to be equal to $-1/2$ in the Pfirsch-Schlüter regime [40, 47].

This expression eq. (46) agrees with Hirshman-Sigmar [40, 47]. It must be noted that the rule $\left\langle BV_{\parallel Z} \right\rangle_\psi = \left\langle BV_{\parallel i} \right\rangle_\psi$ is not very accurate without external sources of momentum. Fülöp and Helander [23] showed that diamagnetic corrections are important. It turns out that the Hirshman-Sigmar result still holds in the case where impurity poloidal asymmetries are small. When they are accounted for, large differences are found in the coefficients (diffusion and screening factor) of the impurity flux [22, 23, 24].

3. Neoclassical transport in the 3 collisionality regimes

The objective of this section is to benchmark the implemented collision operator against the predictions of neoclassical theory regarding the impurity flux, eq. (46). Three neoclassical predictions will be checked hereafter:

- the dependence of D_z^{neo} with respect to the collisionality ν_z^*,
- the dependence of the pinch velocity V_z^{pinch} with respect to the impurity effective charge Z,
- the thermal screening factor H_z^{neo} in the Pfirsch-Schlüter regime.

To this end, purely neoclassical impurity transport is studied with the GYSELA code by performing *axisymmetric* simulations. This means that all non-axisymmetric modes ($n \neq 0$, with n the toroidal mode number) are filtered out at each time step, thus preventing any turbulence to develop, whatever the temperature and density gradients. The main ion species is deuterium. Three different impurities are considered: helium ($A_{He} = 4$), carbon ($A_C = 12$) and tungsten ($A_W = 184$). A single ionization state is considered for each of them: helium and carbon are assumed fully ionized ($Z_{He} = 2, Z_C = 6$), and tungsten only partially ($Z_W = 40$). The collisionality of deuterium is chosen equal to $\nu_D^* = 0.1$ at the center of the simulation domain, denoted r_p. Assuming equal temperatures, the collisionality of the various impurities scales like $\nu_z^* \approx \sqrt{2}\,(Z_z/Z_D)^2\,(A_D/A_z)^{1/2}\,\nu_D^* = 2\nu_D^*\,Z_z^2/A_z^{1/2}$, with $z = \{He, C, W\}$. The collisionalities at mid-radius are given in Table 1. With this choice of ν_D^*, it appears that they cover the entire range of the collisionality regimes: while deuterium and helium are in the banana regime, carbon is in the plateau regime, and tungsten in the Pfirsch-Schlüter regime. The collisionality profiles are plotted on Fig. 1. These impurities are kept at a trace level, i.e. such that the ratio $\alpha = (n_z Z_z^2/n_D Z_D^2)$ is much smaller than unity. Taking this ratio of the order of $\alpha \approx 10^{-3}$ leads to the concentrations listed in Table 1.

A simulation with deuterium only (without any impurity) is first run on about one collision time so as to reach neoclassical equilibrium. It is then restarted with the addition of the chosen impurity. These simulations are performed at the reference (i.e. for hydrogen) normalized gyroradius value equal to $\rho_{*0} = \rho_H/a = 1/150 \approx 6.67\,10^{-3}$. Assuming equal temperatures, the ρ_* values of deuterium and of the chosen impurities then scale like $\rho_{*z} = (A_z^{1/2}/Z_z)\,\rho_{*0}$. The corresponding values are given in Table 1. The aspect ratio is 3.2, and the safety factor typically ranges from 1.5 to 2.5. The number of grid points is the following: $(N_r, N_\theta, N_\varphi) = (256, 256, 32)$, $N_{v_\parallel} = 128 \rightarrow 256$, and $N_\mu = 16 \rightarrow 32$. Note that N_φ is increased up to 128 in the case of turbulent simulations, discussed in section 4.

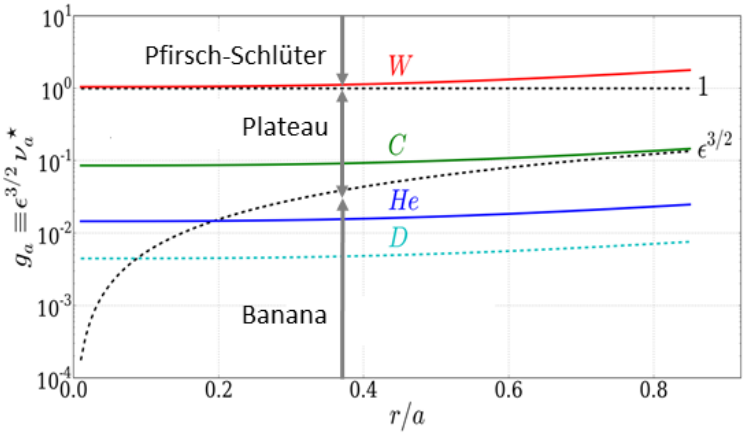

Figure 1. For a given radial profile of deuterium collisionality (blue dashed line), corresponding profiles of the collisionality of 3 trace impurities: helium (He), carbon (C) and tungsten (W, $Z_W = 40$ here). The limits of the three collisionality regimes (banana, plateau, Pfirsch-Schlüter) are also displayed.

Species	D	He	C	W
Collisionality ν_z^*	0.1	0.4	~ 2.1	~ 23.6
Concentration c_z	1	2.10^{-4}	10^{-5}	4.10^{-6}
Norm. gyroradius ρ_{*z}	$\sim 9.43\,10^{-3}$	$\sim 6.67\,10^{-3}$	$\sim 3.85\,10^{-3}$	$\sim 2.26\,10^{-3}$

Table 1. Collisionality, concentration and ρ_* value of the 4 species of the various simulations discussed in the paper. The values are given at the center of the radial domain.

3.1. Diffusion and pinch velocity

The first component of the impurity flux to be studied is the diffusion coefficient D_z. The only non-vanishing gradient is the impurity density gradient $\partial_r N_{Z,eq}$. A single simulation would typically require to run on a particle confinement time to allow one to extract accurately the D_z value. So as to save computation time, three simulations have been run at three different values of $R/L_{n_z} = \{0.7; 1.4; 2.1\}$, measured at r_p (with $1/L_{n_z} = -\partial_r \ln N_{Z,eq}$). The profiles are plotted on Fig. 2 (left). Once the impurity has been injected, and after a short reorganization time, the impurity flux reaches a well defined value, which slowly decreases in time with R/L_{n_z}. The value recorded at r_p is plotted on Fig. 2 (right) for the 3 impurities and the 3 gradients. The impurity flux contains both contributions of the $E \times B$ drift and of the magnetic (curvature and ∇B) drift. Each series of points defines a line that passes by zero, as it should. The slope, equal to D_z, is obtained by a least squares fit.

On Fig. 3, the D_z values obtained with GYSELA in this way are successfully compared with the ones predicted by Hirshman-Sigmar [45] and the ones obtained with the NEO code [48] (adiabatic electrons, Hirshman-Sigmar type of collision operator).

So as to estimate the pinch velocity, a non-vanishing value of the deuterium density

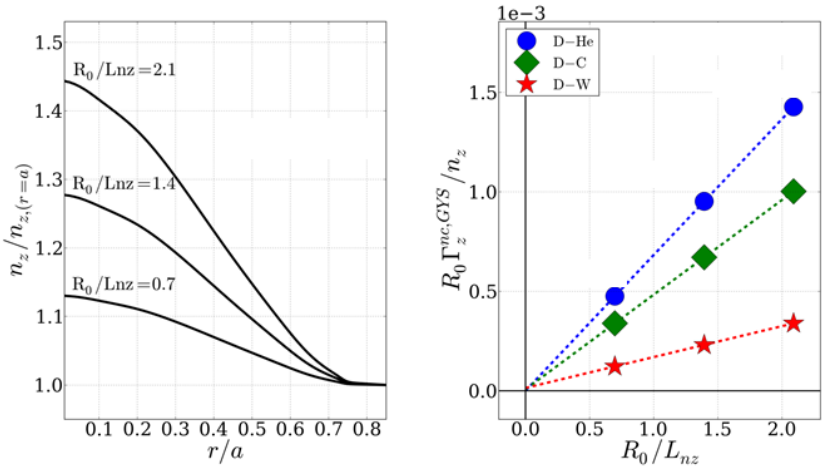

Figure 2. Left: the 3 impurity density profiles considered for GYSELA simulations. Right: the time averaged neoclassical flux computed for each of these profiles is plotted versus the normalized density gradient in the case of 3 impurities (He, C and W) in a deuterium plasma. The slope gives the neoclassical diffusion coefficient.

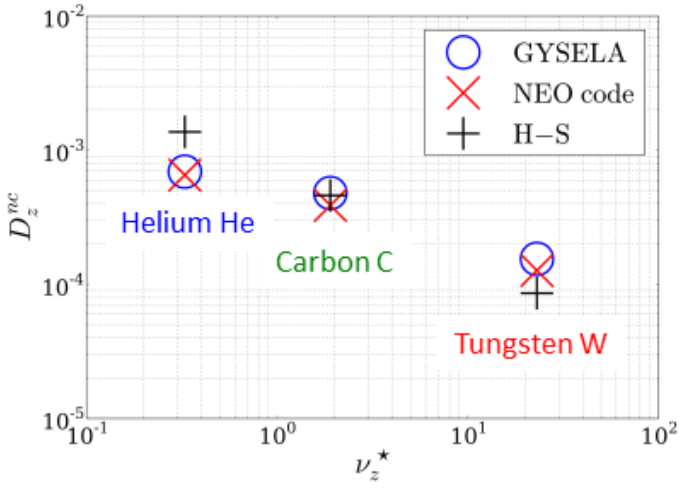

Figure 3. Diffusion coefficient of 3 impurities (He, C and W) in a deuterium plasma versus the impurity collisionality ν_z^*. The GYSELA results (o) are compared with the values predicted by Hirshman-Sigmar [45] (+) and the ones obtained with the NEO code (x).

gradient is considered in addition to $\partial_r N_{Z,eq}$. The deuterium density profile is homothetic to the one of impurities, with $R/L_{n_D} = 0.7$ at r_p. The steady state impurity density profiles would be obtained when the flux vanishes (points on the x-axis on Fig. 4). In this case, they can reveal extremely peaked, as a result of ambipolarity. Indeed, they scale as $N_{Z,eq}/N_{Z,eq}(r=a) = (N_{i,eq}/N_{i,eq}(r=a))^{Z_z}$. In the case of tungsten ($Z_W = 40$), such a strongly peaked profile would require prohibitive numerical resources, namely large number of radial grid points. Also, too short density gradient lengths L_{nz} can conflict with one of the gyrokinetic assumptions, stating that $\rho_z/L_{nz} \ll 1$. Conversely, using the same procedure as the one used for the diffusion coefficient does not suffer

such difficulties.

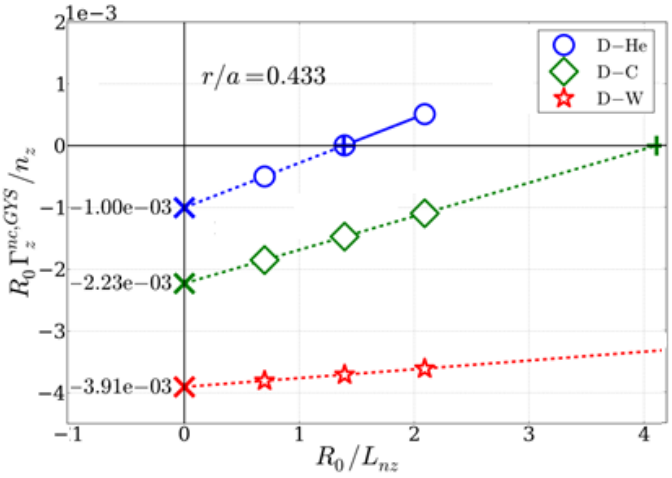

Figure 4. Detail of the method used to retrieve the pinch velocity of 3 impurities (He, C and W) in a deuterium plasma (no temperature gradient). The slope provides the diffusion coefficient, the intersection with the y-axis gives the pinch velocity. Intersection points with the x-axis correspond to the expected equilibrium gradient of the impurity density profiles as a result of the sole main ion density gradient (density peaking).

Figure 4 shows the results of the 9 simulations. The extrapolated values on the y-axis provide the estimate of pinch velocities in GYSELA. These values are plotted on Fig. 5 as a function of collisionality. Theoretically, the normalized pinch velocity is expected to scale like $RV_z^{pinch}/D_z^{neo} = -Z_z R/L_{nD}$. The scaling with collisionality ν_z^* as well as the magnitude of the pinch velocity are successfully recovered.

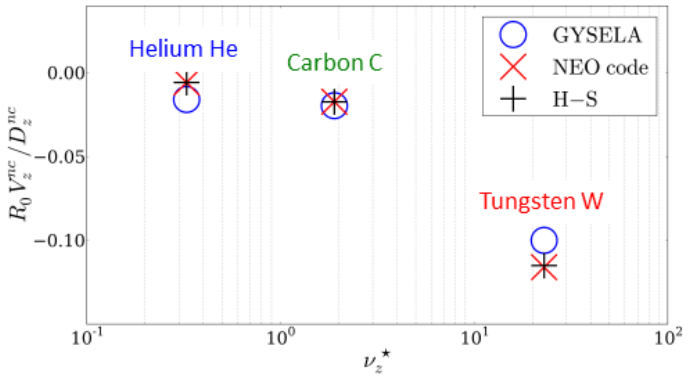

Figure 5. Normalized pinch velocity of 3 impurities (He, C and W) in a deuterium plasma versus the impurity collisionality ν_z^*. The GYSELA results (o) are compared with the values predicted by Hirshman-Sigmar (+) and the ones obtained with the NEO code (x).

3.2. Thermal screening in the P-S regime

When the main ion species exhibits a non-vanishing temperature gradient, there is an additional contribution to the convective part of the flux, due to thermodiffusion. It is expressed in terms of the neoclassical thermal screening factor H_z^{neo} (cf. eq. (46)): $V_z^{thermo} = Z_z\, D_z^{neo} H_z^{neo}\, \nabla_r \log T$. The associated velocity is expected to be outwards (positive) in the Pfirsch-Schlüter regime, for which the value $H_z^{neo} = -1/2$ is commonly admitted (limit of large aspect ratio, provided ν_* is not too large [48]). Should tungsten transport be governed by neoclassical physics in the Pfirsch-Schlüter regime, this term could reveal essential to prevent its accumulation in the core of tokamak plasmas, where its strong radiation critically limits fusion performance. Evidence of impurity outward flow due to thermal screening has already been reported experimentally for low- to medium-Z (helium, nitrogen, neon) materials [49]. Some of the observed outflow of impurities when applying Electron Cyclotron Resonant Heating could well proceed from the same physics [50].

A deuterium-tungsten simulation has been performed with equal initial density and temperature gradient lengths: $R/L_{nD} = R/L_{nW} = 0.1$ and $R/L_{TD} = R/L_{TW} = 1$. Also, temperatures are the same. In this case, the tungsten neoclassical flux is mostly governed by the density and temperature gradients of deuterium only, because they are weighted by the charge of tungsten $Z_W = 40$ (cf. eq. (46)). The following procedure is used to retrieve the thermal screening factor H_W^{neo} from the GYSELA simulation. The neoclassical diffusion coefficient is assumed to be equal to the Hirshman-Sigmar theoretical prediction [45]. Given the actual density and temperature gradients, H_W^{neo} is then such that the right hand side of eq. (46) matches the measured tungsten flux. Notice that the finite discrepancy between D_W^{neo} found in GYSELA simulations and the one predicted by the theory (cf. Fig. 3) impacts the evaluation of H_W^{neo} with the adopted method. The theoretical screening factor integrates the contributions from the various regimes, namely "banana-plateau" (BP) and Pfirsch-Schlüter (PS):

$$H_W = \frac{D_W^{BP} H_W^{BP} + D_W^{PS} H_W^{PS}}{D_W^{BP} + D_W^{PS}} \tag{47}$$

It is plotted on Fig. 6 (red line), where it appears to be dominated by the PS contribution. Its slight departure from $-1/2$ is mainly due to the finite value of ϵ ($\epsilon \simeq 0.13$ at r_p). At $r/a = 0.45$, it is compared a with 2 NEO simulations using two different versions of the collision operator (cf. Tab. 2): the most advanced one (Fokker-Planck), and the one retaining only the pitch-angle part. The latter one corresponds to the limit in which the analytical predictions have been made. It already appears that there is a mismatch between both (pitch-angle NEO and analytic theory), of the order of 18%. Part of the explanation likely comes from the $\epsilon \to 0$ limit which is considered in the analytical derivation: corrections of order $\epsilon^{1/2}$, which is equal to $\sqrt{0.13} \sim 0.36$ in the present case, would be expected. Also, the F-P operator leads to a less effective screening than analytically predicted. This is detrimental to fusion performance: temperature gradients might well be less efficient in screening the natural peaking effect of high Z impurities.

Overall, as expected, the screening factor obtained with GYSELA is negative, i.e. leads effectively to an outward transport of tungsten. It has also the right order of magnitude, although it is about 34% smaller than the NEO prediction with the F-P operator. As already stated, part of this discrepancy is due to the uncertainty regarding the diffusion coefficient D_W^{neo}.

	GYSELA	NEO (Fokker-Planck)	NEO (pitch-angle)	Theory (H-S)
H_W value:	-0.211	-0.321	-0.377	-0.461

Table 2. Thermal screening factor H_W for the D-W case at $r/a = 0.45$.

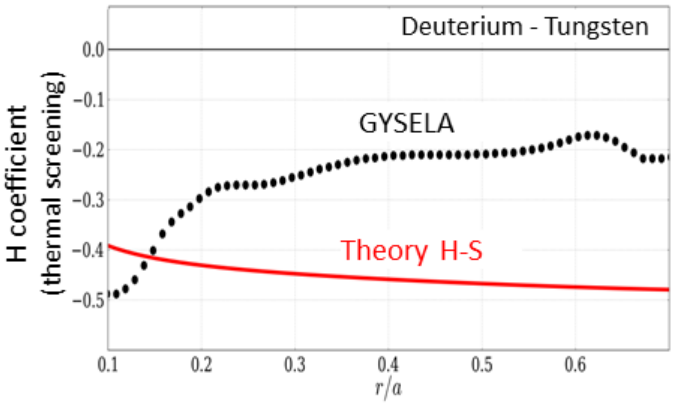

Figure 6. Profile of the thermal screening factor H from a D-W simulation of GYSELA (dots) compared to the value predicted by Hirshman-Sigmar (line).

We review hereafter some of the foundations of the neoclassical theory in the P-S regime, on which rely the derivation of H_z^{neo}, among others.

One of the important results of neoclassical theory in the P-S regime is that the parallel velocities and heat fluxes exhibit a poloidal left-right asymmetry due to the magnetic field inhomogeneity. This asymmetry, due the inhomogeneity of the magnetic field, is responsible for their parallel compressibility. Besides, the asymmetry scales with the pressure and temperature gradients, as evident in eqs. (35),(37). The poloidally fluctuating part of the parallel deuterium (left) and tungsten (middle) velocities are plotted on Fig. 7, as well as that of the deuterium parallel flux (right). The top row shows the instantaneous 2-dimensional values of these fields at the end of the simulation. The bottom row corresponds to the expected asymmetry, proportional to $(1/B - B/\langle B^2\rangle_\psi)$ and weighted by the radial gradients. The agreement between the modeling (top row) and theoretical results (bottom row) looks satisfactory, both in terms of magnitude and in shape. With the adopted collision operator, parallel flows in GYSELA turn out to exhibit the right structure.

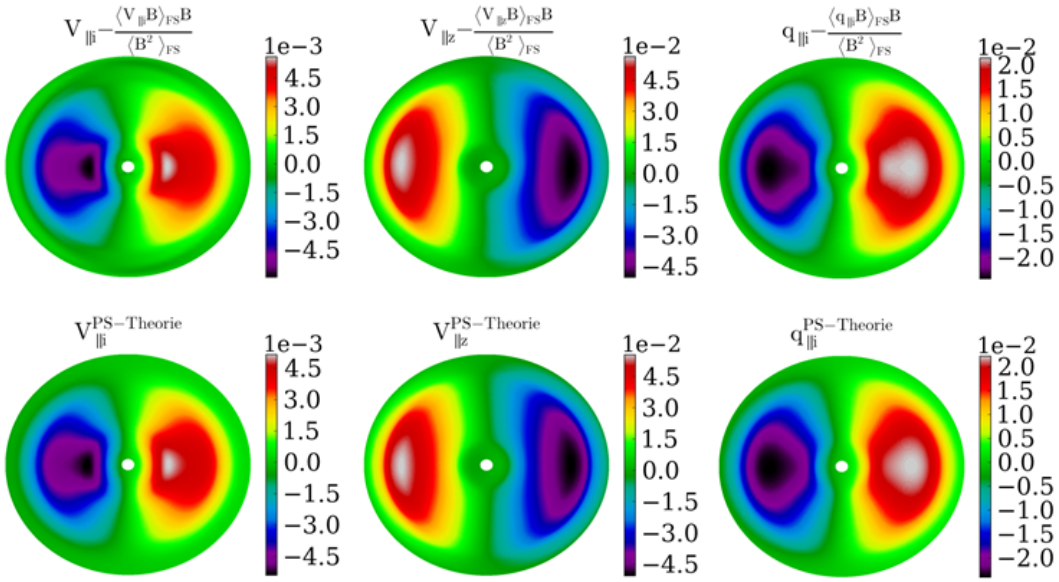

Figure 7. Top row: poloidal fluctuations of the actual parallel velocities and flux obtained with GYSELA. Bottom row: same quantity computed from the radial gradients (cf. eqs.(36-38)). The agreement between theory and modeling looks satisfactory.

In summary, this set of purely neoclassical simulations − where the sole axisymmetric modes $n = 0$ have been retained − has shown that the reduced collision operator implemented in GYSELA, eq. (21), allows one to recover the main results of the neoclassical theory regarding impurity transport in all three collisionality regimes, banana, plateau and Pfirsch-Schlüter. This includes the diffusion coefficient, the pinch velocity due to the main ion density gradient, and the thermal screening factor due to the main ion temperature gradient. This latter term has been found to slightly depart from the analytical estimate, which is close to $H_Z = -1/2$ in the Pfirsch-Schlüter regime. The reason is twofold. Firstly, numerical simulations with the dedicated neoclassical code NEO also predict a negative value for H_Z, but closer to zero. This strongly suggests that the analytical estimate is probably too optimistic. Secondly, the uncertainties in the determination of the diffusion coefficient in GYSELA do affect the computed value of H_Z. The next section explores the interplay between neoclassical and turbulent channels for impurity transport.

4. Evidence of synergy between neoclassical and turbulent impurity transport

In tokamak plasmas, the radial transport of matter and energy, governed by collisions and turbulence, is intrinsically multi scales. While neoclassical transport results from stationary large scale structures, namely static $(m, n) = (1, 0)$ modes (m, n being the poloidal and toroidal Fourier wave numbers, respectively), turbulence develops fluctuating small scale modes $m, n \gg 1$. On the basis of this scale separation, it is usually

assumed that both contributions are additive. In turn, these two transport channels are modeled with different dedicated codes (see e.g. [5, 6, 7, 52, 12]). One of the key questions is whether this assumption is valid, or whether neoclassical and turbulent transports exhibit synergistic effects.

This section gives the first evidence of synergistic effects between neoclassical physics and ITG (Ion Temperature Gradient) turbulence with respect to impurity transport. Previous evidences of such a synergy have been reported in the literature. They deal with poloidal flow [51], heat transport [53, 54] and parallel momentum transport [36, 55]. Also, drift wave turbulence has been shown analytically to be able to significantly contribute to the bootstrap current through direct modification of the axisymmetric plasma current distribution via turbulence-induced electron detrapping [56]. This mechanism could reveal particularly vigorous during transient bursts of turbulent transport. In all of these studies, identifying any synergy between turbulent and neoclassical transports depends on the definition which is given to both transport channels. Obviously, in experiments − like in self consistent simulations including both turbulence and neoclassical physics − the total flux is simply the sum of turbulence and neoclassical contributions. The question is then the following: can this self-consistent flux be recovered by adding up the fluxes coming from two independent simulations, one dealing with turbulence physics only, the other one with neoclassical physics only? If the answer is "No", this means that both channels then exhibit some kind of synergy, which would remain being understood. The adopted GYSELA set up which led to the conclusion that there exists synergy between these transport channels is detailed in section 4.2.

4.1. Impurity transport in collisional turbulence

The transport of 3 impurities (He, Ne and W) is studied in the ITG turbulent regime. They find themselves in the three regimes of neoclassical transport, namely banana, plateau and Pfirsch-Schlüter, respectively. The total impurity flux is then the sum of two contributions, carried by the electric and magnetic drifts:

$$\left\langle \Gamma_z^{tot} \right\rangle_\psi = \left\langle \int d^3\mathbf{v}\ F_z\ (\mathbf{v}_{D,z} + \mathbf{v}_{E,z}) \cdot \boldsymbol{\nabla} r \right\rangle_\psi \tag{48}$$

Here, the magnetic $\mathbf{v}_{D,z}$ and electric $\mathbf{v}_{E,z}$ drifts are defined by:

$$\mathbf{v}_{D,z} = \frac{m_z v_{G\|}^2 + \mu_z B}{ZeB_{||}^*}\ \frac{\mathbf{b} \times \boldsymbol{\nabla} B}{B} \tag{49}$$

$$\mathbf{v}_{E,z} = \frac{\mathbf{b} \times \boldsymbol{\nabla}(J_z.\phi)}{B_{||}^*} \tag{50}$$

with $\mathbf{b} = \mathbf{B}/B$ and J_z the gyro-average operator. There is not a one-to-one correspondence between these two contributions, those of the magnetic and electric drifts on the one hand, and the definitions of the neoclassical and turbulent fluxes on

the other hand. Indeed, part of the neoclassical flux is carried by the electric drift, more precisely by its axi-symmetric component $n = 0$. This point will be taken into account when looking for possible synergies between neoclassical and turbulent transports, in section 4.2.

The simulations are performed as follows. They consist in two consecutive phases. First, GYSELA is run in the single-species mode, evolving the distribution function of the main ion (deuterium) only, until the saturated regime of turbulence is reached. This phase typically lasts several tens of turbulence auto-correlation times. In a second phase, the simulation is restarted in the two-species mode, where the full distribution functions of deuterium f_D and impurity f_z are self-consistently advanced in time. In the present cases, there is no source of particles. Impurities are initialized with a density profile n_z homothetic to the one of deuterium n_D, but at low concentration ($c_z = n_z/n_{e0} \ll 1$, with n_{e0} the constant-in-time electron density) so that the impurity remains at a trace level. Although this is not critical for trace impurities, the deuterium concentration is reduced in the quasi-neutrality equation, so that the sum $(c_D + Zc_z)$ remains equal to one. By doing so, one ensures that no charge is injected in the system.

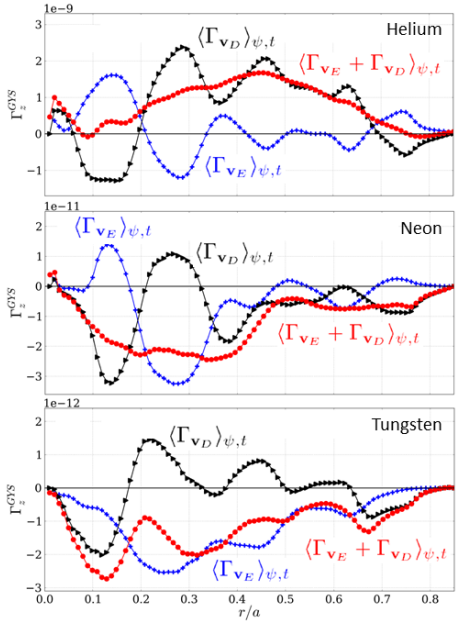

Figure 8. Time and flux-surface average of the radial impurity flux in D-Helium, D-Neon and D-Tungsten simulations. The total flux (red) is decomposed into its electric (blue) and magnetic (black) drift components.

The flux-surface average of the radial impurity flux is plotted in Fig. 8 for each of the 3 simulations. It is time-averaged on several turbulence correlation times during the turbulence saturation phase. Two main observations can be made. First, the fluxes carried by the electric and magnetic drifts are of the same order of magnitude, and tend to compensate each other. This trend seems to be more pronounced for the

lighter impurity, helium. Such a behavior has also been reported for parallel momentum transport [36, 55], although no clear explanation has been proposed so far. Second, this compensation is however not complete so that, for this set of parameters, the total flux is outward for helium, and inward for neon and tungsten. This latter observation is potentially detrimental to fusion performance in tungsten divertor machines like WEST and ITER, but a more systematic study as function of plasma parameters is clearly needed. This is left for future work.

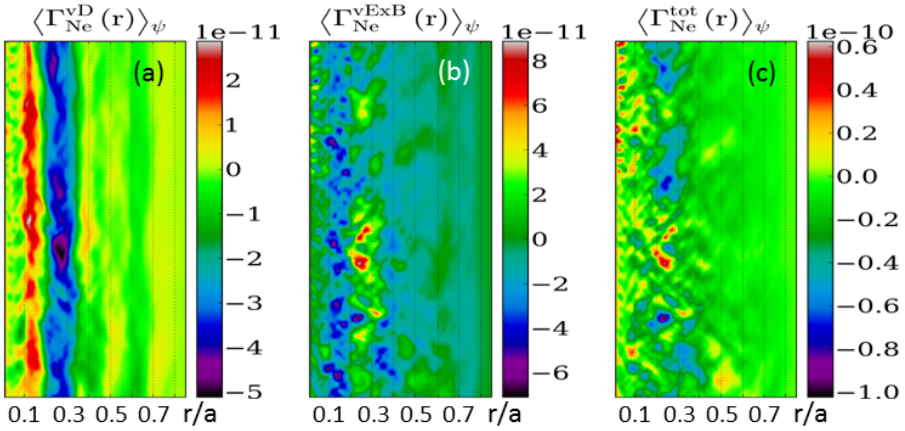

Figure 9. Flux-surface average of the neon radial flux as a function of time and normalized radius. The total flux (c) is decomposed into its electric (b) and magnetic (a) drift components.

Interestingly, as evident on Fig. 9, the magnetic (a) and electric (b) drift components exhibit a rich dynamics: the former due to the turbulent fluctuations of the electric potential, the latter due to the dynamics of both the corrugated equilibrium gradients and of the $m = 1$ modes (see below). As a result, the total flux Fig. 9(c) features complex dynamical patterns, with large deviations from the mean: small scale avalanche-like events can even lead, locally and temporarily, to the sign reversal of the flux.

4.2. Evidence of synergies

The level − and existence − of synergy between neoclassical and turbulent transports largely relies on the definition of these two terms. Obviously, in experiments as well as in self-consistent simulations, the total flux is the sum of neoclassical and turbulent contributions. Then how to capture any possible synergy? This question makes sense when realizing that present estimates of these two transports are performed with different dedicated numerical codes. Then, our strategy aims at assessing whether, and in which regimes, the total flux can effectively be simply obtained by adding up the numerical calculations which are currently performed in the literature. GYSELA allows one to run reduced sets of simulations, either retaining the sole neoclassical contribution or the turbulent one, to be compared to self-consistent simulations where neoclassical and turbulent transports are treated on an equal footing.

In that spirit, for each of the 3 considered trace impurities He, Ne and W, 3 simulations have been performed:

(i) Purely neoclassical (called "neoclassical" hereafter): in this case, all non-axisymmetric toroidal modes are filtered out at each time step (i.e. all Fourier modes with $n \neq 0$ are set to zero, with n the toroidal mode number). The neoclassical flux is then the sum of both $E \times B$ and magnetic drift contributions (the need to account for both terms is consistent with neoclassical theory, as discussed in [57, 58]):

$$\langle \Gamma_z^{neo} \rangle_\psi = \left\langle \int d^3\mathbf{v}\ F_z\ (\mathbf{v}_{D,z} + \mathbf{v}_{E,z}^{n=0}) \cdot \boldsymbol{\nabla} r) \right\rangle_\psi \tag{51}$$

This definition departs from the more common understanding where neoclassical transport is carried by the magnetic drift $\mathbf{v}_{D,z}$ only.

(ii) Mainly turbulent (called "turbulent" hereafter): in this case, single-species collisions only are retained (namely ν_{ii} and ν_{zz}) , so that momentum or energy exchange between species is not taken into account. The fact that $\nu_{Zi} = 0$ in this simulation implies that the parallel friction force is also vanishing: $R_{\parallel Zi} = 0$. As a result, in virtue of eq. (30), the radial neoclassical flux is exactly zero. Retaining intra-species collisions is however important and sufficient to account, among others, for the collisional damping of zonal flows, which are known to contribute efficiently to turbulence saturation. In the case of trace impurities, the collision operator for the main ions only is important. Indeed, impurity-impurity collisions are negligible in this case. The turbulent flux is then governed by the electric drift:

$$\left\langle \Gamma_z^{turb} \right\rangle_\psi = \left\langle \int d^3\mathbf{v}\ F_z\ (\mathbf{v}_{E,z} \cdot \boldsymbol{\nabla} r) \right\rangle_\psi \tag{52}$$

(iii) Full (called "total" hereafter): in this case, no simplification is made to the collision operator, nor any filtering applied to the electric potential. More precisely, all terms of the collision operator are retained, involving both intra- and inter-species collisions, in the turbulent regime.

As an example, the case of tungsten is considered hereafter. The same trend is observed for the two other impurities. In Fig. 10, the total tungsten flux (red) from the self-consistent simulation is compared to the sum of the neoclassical and turbulent fluxes (black), coming from the reduced simulations. First, conversely to the magnetic and electric drift components of the flux, the neoclassical and turbulent contributions do not exhibit any clear sign of partial compensation. Second, the total flux of tungsten turns out to be inward in this case. However, this result should not be considered as a general statement. A thorough exploration of the parameter space (including density and temperature gradients, collisionality and the source of tungsten) should be performed before reaching more general conclusions. This is left for future work. Third and most importantly, it appears that the total flux differs from the sum of the neoclassical and turbulent fluxes, by more than a factor two at some radial locations.

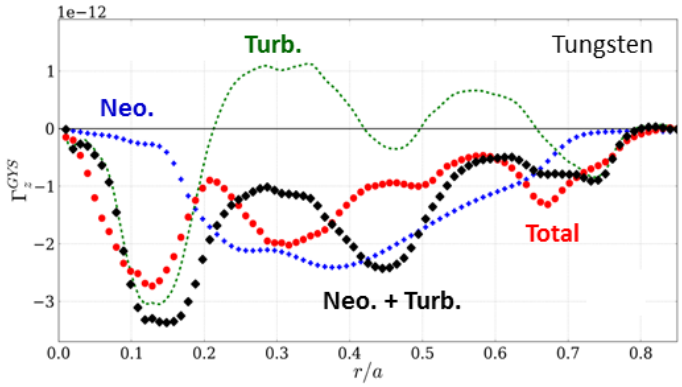

Figure 10. Time-averaged radial tungsten flux in neoclassical (blue), turbulent (green) and full (red) simulations. The sum of the fluxes of the neoclassical and turbulent simulations is shown in black.

This result shows that *neoclassical and turbulent impurity transports are not additive*, in the sense that they cannot be computed separately and then simply added up.

One of the explanations of this synergy comes from the impact of turbulence on the magnitude and radial shape of poloidal asymmetries, i.e. of the $m = 1$ Fourier mode. Indeed, in/out asymmetries of the impurity density profile are able to greatly modify neoclassical coefficients, up to one or two orders of magnitude, as predicted theoretically [22, 23, 24, 25]. The time-averaged $(m, n) = (1, 0)$ component of the electric potential (actually, this is not exactly the $n = 0$ component: the Fourier transform is performed at a given toroidal location. However, the $m = 1$ spectrum exhibits a large peak at $n = 0$, so that the axisymmetric mode is dominant) is plotted on Fig. 11, for the three simulations with tungsten: neoclassical, turbulent and total. The magnitude of the $(1, 0)$ mode is larger in the presence of turbulence, and exhibits smaller radial scales (b,c) than in the neoclassical case (a). Its magnitude turns out to be of the order of $\rho_* = 1/150$.

In these simulations, the parallel Mach number of the main ion $M_{\|D}$ is fairly small, so that the one of tungsten does not exceed 10% ($M_{\|W} \approx (A_W/A_D)^{1/2} M_{\|D}$). In this case, centrifugal effects are sub-dominant. One thus expects tungsten density fluctuations to have an adiabatic response, namely $\delta N_W/\langle N_W\rangle_{FS} \equiv N_W/\langle N_W\rangle_{FS} - 1 \sim -Z(e\,\delta\phi/T_Z)$ [6]. As a matter of fact, this is exactly the order of magnitude which is obtained in this simulation, as evident on Fig. 12(b). There, the large scale $m = 1$ mode emerges from the small scale turbulent structures. Interestingly, δN_W peaks at about $4.5\,10^{-8}$, while the flux-surface averaged tungsten density (not shown here) is about $1.1\,10^{-7}$. The ratio $\delta N_W/\langle N_W\rangle_{FS}$ is well in the expected range $Z(e\,\delta\phi/T_Z) \approx 0.4$. Further notice that the poloidal asymmetry is larger in the turbulent regime than in the purely neoclassical simulation, Fig. 12(a), the extrema being larger by 40% to 80%.

In summary, the large scale poloidal structures of the impurity density, which are generated by turbulence (via the turbulence-induced $m = 1$ mode of the electric

potential), add-up and/or compete with those governed by neoclassical physics, so that neoclassical and turbulent transports are not additive (in the sense already defined). A more systematic exploration of the parameter space, especially in terms of temperature and density gradients, as well as the charge and mass of the impurity, is currently performed to assess the conditions for and magnitude of this synergy. This will be the subject of a forthcoming paper, including a more detailed analysis of the mechanism for this synergy (including possible kinetic effects).

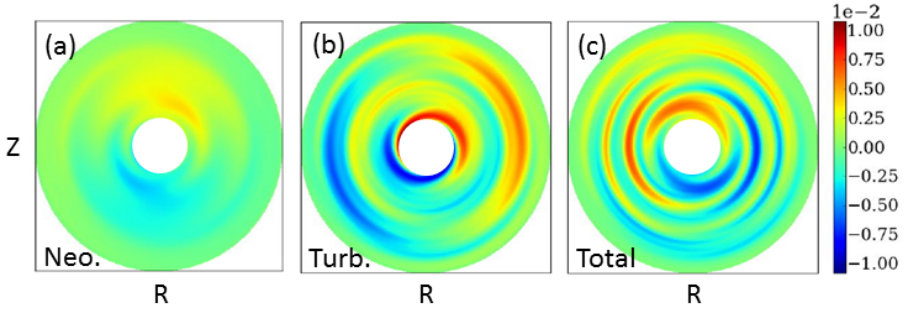

Figure 11. Time-averaged poloidal cross-sections of the $(m, n) = (1, 0)$ component of the electric potential for the 3 simulations in the case of a deuterium-tungsten plasma.

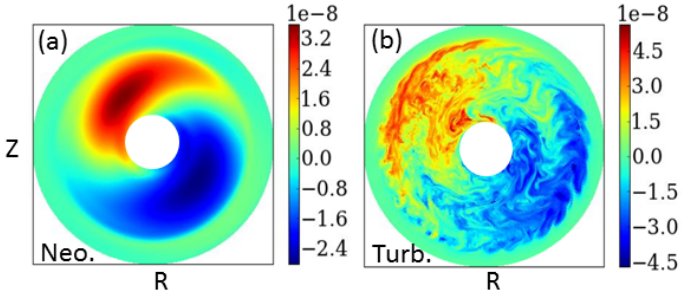

Figure 12. Instantaneous poloidal cross-sections of tungsten density fluctuations $\delta N_W = N_W - \langle N_W \rangle_{FS}$ (with $\langle ... \rangle_{FS}$ the flux-surface average) for the 2 reduced simulations in the case of a deuterium-tungsten plasma.

5. Conclusions

Impurity transport is likely to play a key role in limiting ITER performance. ITER plasmas will face intrinsic impurities with helium ashes, and extrinsic impurity influxes due to either edge impurity seeding (neon, argon) which aim at radiating most of the power or due to plasma-wall interaction (tungsten, beryllium). The case of tungsten is particularly severe, since core accumulation leads to strong radiation that can prevent the access to high performance discharges, and can even lead to radiative collapses. Quantitative predictions of impurity transport is therefore critical, as well as the search for possible control mechanisms to prevent too large impurity concentration in the plasma core.

Both collisional (neoclassical) and turbulent transport contribute to the impurity flux. Their respective magnitude depends mainly on the mass and charge state of the impurity, on the main ion density and temperature gradients, on the level (with or without transport barrier) and nature (e.g. ITG versus TEM) of turbulence, and on the heating scheme (isotropic or not, with or without torque injection). It is suspected that both transport channels could exhibit similar magnitudes in ITER plasmas for high-Z impurities like tungsten.

The flux-driven gyrokinetic GYSELA code is used to study impurity transport without any scale separation assumption between neoclassical and turbulent transport channels. Conversely to the usual hypothesis that they are uncorrelated and additive, both are treated on an equal footing in GYSELA. The implemented multi-species collision operator has been shown analytically to allow one to recover neoclassical predictions for impurity transport in the Pfirsch-Schlüter regime. The impurity flux of purely neoclassical simulations (performed by filtering out non-axisymmetric modes) of deuterium plasmas with trace impurities of helium, carbon and tungsten has been successfully benchmarked with respect to both neoclassical theory and NEO simulations in the three collisionality regimes. Especially, the neoclassical diffusion coefficient, the inward pinch velocity due to density peaking, and the thermo-diffusive contribution have been recovered. Interestingly, it appears that the thermal screening coefficient departs from the analytical estimate of $-1/2$ in the Pfirsch-Schlüter regime. The computed screening efficiency is less, which is detrimental to fusion performance. Finally, first nonlinear simulations in the turbulent regime show that the self-consistently computed impurity flux is not the sum of turbulent and neoclassical contributions computed independently, as usually assumed in the literature. The mismatch can reach up to a factor of two at some radial locations. The discrepancy comes from the excitation of $(m, n) = (\pm 1, 0)$ modes of the electric potential by turbulence, resulting in turbulence-driven in-out poloidal asymmetries of the impurity density profile. Forthcoming simulations will explore and quantify this synergy in a more systematic way by scanning the parameter space. Such results put already forward the need for self-consistent simulations of impurity transport in view of providing quantitative predictions for ITER.

Acknowledgments

The authors acknowledge the fruitful and lively discussions held during the 8th Festival de Théorie, held in Aix-en-Provence, July 2015. This work was granted access to the national HPC resources of CCRT, CINES, and IDRIS under GENCI (Grand Equipement National de Calcul Intensif) allocations and also with Helios/IFERC machine dedicated to Fusion at Rokkasho in Japan and with PRACE (Partnership for Advanced Computing in Europe) Research infrastructure. This project has received funding from the European Union's Horizon 2020 research and innovation program under Grant Agreement No. 633053. The views and opinions expressed herein do not

necessarily reflect those of the European Commission.

Appendix A. Collision operator: details

The diffusion coefficients in the velocity $D_{v,ab}$ is related to the deflection collision frequencies $\nu_{d,ab}$ via the relation

$$D_{d,ab}(v) = \frac{1}{2}\nu_{d,ab}(v)v^2 = v_{Ta}^2 x_a^2 \nu_{d,ab}(x_a) \tag{A.1}$$

where v is the velocity modulus (i.e. $E = \frac{1}{2}m_a v^2$) and x_a is a normalized velocity modulus

$$x_a = \sqrt{\frac{E}{T_a}} = \frac{v}{\sqrt{2}v_{Ta}} \tag{A.2}$$

We introduce a normalizing self-collision frequency ν_{aa} for the species 'a'

$$\nu_{aa} = \frac{4\sqrt{\pi}}{3}\frac{\ln\Lambda}{(4\pi\varepsilon_0)^2}\frac{N_a Z_a^4 e^4}{m_a^2 v_{Ta}^3} \tag{A.3}$$

With these notations, the velocity, deflection and slowing-down collision frequencies are

$$\nu_{d,ab}(x_a) = \nu_{ab}^{HS}\frac{v_{Ta}}{v_{Tb}}\frac{\Psi(x_b)}{x_a^2} \tag{A.4}$$

$$\nu_{s,ab}(v) = \nu_{ab}^{HS}\frac{T_a}{T_b}\left(1+\frac{m_b}{m_a}\right)\frac{v_{Ta}}{v_{Tb}}\Theta(x_b) \tag{A.5}$$

where

$$\nu_{ab}^{HS} = \sqrt{2}\frac{N_b Z_b^2}{N_a Z_a^2}\nu_{aa} \tag{A.6}$$

Here x_b is a function of x_a, i.e.

$$x_a = \frac{v}{\sqrt{2}v_{Ta}} \tag{A.7}$$

$$x_b = x_{ba}x_a = \frac{v}{\sqrt{2}v_{Tb}} \tag{A.8}$$

$$x_{ba} = \frac{v_{Ta}}{v_{Tb}} \tag{A.9}$$

The functions Ψ, G, Φ depend on the velocity modulus only and are defined as

$$\Psi(x) = \frac{3\sqrt{\pi}}{4}\frac{1}{x}\left[\Phi(x) - G(x)\right] \tag{A.10}$$

$$\Theta(x) = \frac{3\sqrt{\pi}}{2}\frac{G(x)}{x} \tag{A.11}$$

$$G(x) = \frac{1}{2x^2}\left(\Phi(x) - x\Phi'(x)\right) \tag{A.12}$$

$$\Phi(x) = \frac{2}{\sqrt{\pi}}\int_0^x dy \exp\left(-y^2\right) \tag{A.13}$$

The function $\Phi(x)$ is the error function, and the function $G(x)$ is the Chandrasekhar function, in accordance with Hirshman-Sigmar [45, 46] and Hinton-Hazeltine [39, 44]

papers. These definitions have been chosen such that the deflection and slowing-down frequencies $\nu_{d,ab}$ and $\nu_{s,ab}$ coincide with the definitions given by Hirshman and Sigmar [45]. The notation ν_{ab}^{HS} refers to the interspecies collision rate $1/\tau_{ab}$ defined in [40, 47]. Hence ν_{ab}^{HS} is different from the inter-species momentum transfer rate ν_{ab}. In particular ν_{aa}^{HS} differs from ν_{aa} by a factor $\sqrt{2}$, i.e. $\nu_{aa}^{HS} = \sqrt{2}\nu_{aa}$. Useful asymptotic limits are

$$\text{slow particle } (x \to 0): \quad \Psi(x) \to 1; \quad \Theta(x) \to 1 \tag{A.14}$$

$$\text{fast particle } (x \to \infty): \quad \Psi(x) \to \tfrac{3\sqrt{\pi}}{4}\tfrac{1}{x}; \quad \Theta(x) \to \tfrac{3\sqrt{\pi}}{4}\tfrac{1}{x^3} \tag{A.15}$$

References

[1] R.A. Pitts, S. Carpentier, F. Escourbiac, T. Hirai, V. Komarov, S. Lisgo, A.S. Kukushkin, A. Loarte, M. Merola, A. Sashal Naik, R. Mitteau, M. Sugihara, B. Bazylev, P.C. Stangeby, *J. Nucl. Mater.* **438** (2012) S48

[2] J. Bucalossi, A. Argouach, V. Basiuk, O. Baulaigue, P. Bayetti, M. Bécoulet, et al., *Fusion Eng. Des.* **86** (2011) 684?688.

[3] A. Grosman, J. Bucalossi, L. Doceul, F. Escourbiac, M. Lipa, M. Merola, M. Missirlian, R.A. Pitts, F. Samaille, E. Tsitrone, *Fusion Eng. Des.* **88** (2012) 497

[4] T. Pütterich, R. Neu, R. Dux, A.D. Whiteford, M.G. O?Mullane, H.P. Summers and the ASDEX Upgrade Team, *Nucl. Fusion* **50**, 025012 (2010)

[5] C. Angioni, P. Mantica, T. P?utterich, M. Valisa, M. Baruzzo, E. A. Belli, P. Belo, F. J. Casson, C. Challis, P. Drewelow, C. Giroud, N. Hawkes, T. C. Hender, J. Hobirk, T. Koskela, L. Lauro Taroni, C. F. Maggi, J. Mlynar, T. Odstrcil, M. L. Reinke, M. Romanelli, and JET EFDA Contributors, *Nucl. Fusion* **54**, 083028 (2014).

[6] F J Casson, C Angioni, E A Belli, R Bilato, P Mantica, T Odstrcil, T Pütterich, M Valisa, L Garzotti, C Giroud, J Hobirk, C F Maggi, J Mlynar, M L Reinke, JET EFDA Contributors and ASDEX-Upgrade Team, *Plasma Phys. Control. Fusion* **57** (2015) 014031

[7] A. Loarte, M. L. Reinke, A. R. Polevoi, M. Hosokawa, M. Chilenski, N. Howard, A. Hubbard, J. W. Hughes, J. E. Rice, J. Walk, Alcator C-Mod Team, F. Köchl, T. Pütterich, R. Dux, and V. E. Zhogolev, *Phys. Plasmas* **22** (2015) 056117

[8] J.E. Rice, J.L. Terry, J.A. Goetz, Y. Wang, E.S. Marmar, M. Greenwald, I. Hutchinson, Y. Takase, S. Wolfe, H. Ohkawa, and A. Hubbard, *Phys. Plasmas* **4** (1997) 1605

[9] R Guirlet, C Giroud, T Parisot, M E Puiatti, C Bourdelle, L Carraro, N Dubuit, X Garbet and P R Thomas, *Plasma Phys. Control. Fusion* **48** (2006) B63

[10] R. Guirlet, D. Villegas, T. Parisot, C. Bourdelle, X. Garbet, F. Imbeaux, D. Mazon, D. Pacella, *Nucl. Fusion* **49** (2009) 055007

[11] D. Villegas, R. Guirlet, C. Bourdelle, G. T. Hoang, X. Garbet, and R. Sabot, *Phys. Rev. Lett.* **105** (2010) 035002

[12] S S Henderson, L Garzotti, F J Casson, D Dickinson, M O?Mullane, A Patel, C M Roach, H P Summers, H Tanabe, M Valovič and the MAST team, *Plasma Phys. Control. Fusion* **57** (2015) 095001

[13] R. Buchholz, S. Grosshauser, W. Guttenfelder, W. A. Hornsby, P. Migliano, A. G. Peeters, and D. Strintzi, *Phys. Plasmas* **22** (2015) 082307

[14] Petrasso R., Sigmar D., Wenzel K., Hopf J., Greenwald M., Terry J., Parker J., *Phys. Rev. Lett.* **57** (1986) 707

[15] Giannella R., Hawkes N., Taroni L. L., Mattioli M., O?Rourke J., Pasini D., *Plasma Phys. Control. Fusion* **34** (1992) 687

[16] Dux R., Giroud, C., Neu R., Peeters A., Stober J., Zastrow K.-D., Team A. U., et al., *J. Nucl. Mater.* **313** (2003) 1150

[17] Takenaga H., Higashijima S., Oyama N., Bruskin L., Koide Y., Ide S., Shirai H., Sakamoto Y., Suzuki T., Hill K. et al., *Nucl. Fusion* **43** (2003) 1235
[18] Dux R., Giroud, C. Zastrow, K.-D. et al., *Nucl. Fusion* **44** (2004), 260
[19] C. Angioni, F. J. Casson, P. Mantica, T. Pütterich, M. Valisa, E. A. Belli, R. Bilato, C. Giroud, P. Helander, and JET Contributors, *Phys. Plasmas* **22** (2015) 055902
[20] J.E. Rice, M.L. Reinke, C. Gao, N.T. Howard, M.A. Chilenski, L. Delgado-Aparicio, R.S. Granetz, M.J. Greenwald, A.E. Hubbard, J.W. Hughes, J.H. Irby, Y. Lin1, E.S. Marmar, R.T. Mumgaard, S.D. Scott, J.L. Terry, J.R. Walk, A.E. White, D.G. Whyte, S.M. Wolfe and S.J. Wukitch, *Nucl. Fusion* **55** (2015) 033014
[21] R Dux, A Loarte, E Fable and A Kukushkin, *Plasma Phys. Control. Fusion* **56** (2014) 124003
[22] M. Romanelli, M. Ottaviani, *Plasma Phys. Control. Fusion* **40** (1998) 1767
[23] F. Fülöp and P. Helander, *Phys. Plasmas* **6**, 3066 (1999).
[24] C. Angioni and P. Helander, *Plasma Phys. Control. Fusion* **56**, 124001 (2014).
[25] E. Belli, J. Candy, C. Angioni, *Plasma Phys. Control. Fusion* **56** (2014) 124002
[26] Wesson J.A., *Nucl. Fusion* **37** (1997) 577
[27] Ingesson L C, Chen H, Helander P and Mantsinen M J, *Plasma Phys. Control. Fusion* **42** (2000) 161
[28] Reinke M et al., *Plasma Phys. Control. Fusion* **54** (2012) 045004
[29] Ye O Kazakov, I Pusztai, T Fülöp and T Johnson, *Plasma Phys. Control. Fusion* **54** (2012) 105010
[30] D. Estève, X. Garbet, Y. Sarazin, V. Grandgirard, T. Cartier-Michaud, G. Dif-Pradalier, P. Ghendrih, G. Latu, C. Norscini, *Phys. Plasmas* **22** (2015) 122506
[31] V. Grandgirard, J. Abiteboul, J. Bigot, T. Cartier-Michaud, N. Crouseilles, G. Dif-Pradalier, Ch. Ehrlacher, D. Esteve, X. Garbet, Ph. Ghendrih, G. Latu, M. Mehrenberger, C. Norscini, Ch. Passeron, F. Rozar, Y. Sarazin, E. Sonnendrücker, A. Strugarek, D. Zarzoso, *Comp. Phys. Commun.* **207**, 35 (2016).
[32] A. J. Brizard and T. S. Hahm, *Rev. Mod. Phys.* **79**, 421 (2007).
[33] X. Garbet, Y. Idomura, L. Villard, T.H. Watanabe, *Nucl. Fusion* **50**, 043002 (2010).
[34] A. J. Brizard, *Phys. Plasmas* **17**, 112503 (2010).
[35] D. Scott and J. Smirnov, *Phys. Plasmas* **17**, 112302 (2010).
[36] J. Abiteboul, X. Garbet, V. Grandgirard, S. J. Allfrey, Ph. Ghendrih, G. Latu, Y. Sarazin, and A. Strugarek, *Phys. Plasmas* **18**, 082503 (2011).
[37] Y. Idomura, *Phys. Plasmas* **21**, 022517 (2014).
[38] R.D. Hazeltine, *Phys. Fluids* **17**, 961 (1974).
[39] F. L. Hinton and R. D. Hazeltine, "Theory of plasma transport in toroidal confinement systems", *Rev. Mod. Phys.* **48**, 239 (1976)
[40] S.P. Hirshman and D.J. Sigmar, *Nucl. Fusion* **21**, 1079 (1981).
[41] Per Helander and Dieter J. Sigmar, "Collisional Transport in Magnetized Plasmas", Cambridge University Press (2005).
[42] S.P. Hirshman, D.J. Sigmar, and J.F. Clarke, *Phys. Fluids* **19**, 656 (1976).
[43] S.P. Hirshman , *Phys. Fluids* **19**, 155 (1976).
[44] F. L. Hinton, "Collisional Transport in Plasma", Basic Plasma Physics vol 1, p. 148, edited by M.N. Rosenbluth and R.Z. Sagdeev, North Holland 1983.
[45] S.P. Hirshman and D.J. Sigmar, *Phys. Fluids* **19**, 1532 (1976).
[46] S.P. Hirshman and D.J. Sigmar, *Phys. Fluids* **20**, 418 (1977).
[47] K.W. Wenzel and D.J. Sigmar, *Nucl. Fusion* **30**, 1117 (1990).
[48] E. Belli and J. Candy, *Plasma Phys. Control. Fusion* **54**, 015015 (2012).
[49] M. R. Wade, W. A. Houlberg, L. R. Baylor, *Phys. Rev. Lett.* **84** (2000) 282
[50] Joohwan Hong, Seung Hun Lee, Juhyung Kim, C.R. Seon, S.G. Lee, G.Y. Park, K.D. Lee, S.S. Henderson, H.Y. Lee, Jae Sun Park, Juhyeok Jang, Siwon Jang, Taemin Jeon, M. O′Mullane and Wonho Choe, *Nucl. Fusion* **55** (2015) 063016

[51] Dif-Pradalier G., Grandgirard V., Sarazin Y., Garbet X., Ghendrih P. (2009), *Phys. Rev. Lett.* **103**, 065002
[52] B. A. Grierson, K. H. Burrell, R. M. Nazikian, W. M. Solomon, A. M. Garofalo, E. A. Belli, G. M. Staebler, M. E. Fenstermacher, G. R. McKee, T. E. Evans, D. M. Orlov, S. P. Smith, C. Chrobak, C. Chrystal, and DIII-D Team, *Phys. Plasmas* **22**, 055901 (2015)
[53] Vernay T., Brunner S., Villard L., McMillan B., Jolliet S., Tran T., Bottino A. (2012), *Phys. Plasmas* **19**, 042301
[54] M. Oberparleiter, F. Jenko, D. Told, H. Doerk, T. Görler, *Phys. Plasmas* **23**, 042509 (2016).
[55] Idomura Y. (2014), *Phys. Plasmas* **21**, 022517
[56] McDevitt C.J., Tang X.-Z., Guo Z. (2013), *Phys. Rev. Lett.* **111**, 205002
[57] T. Vernay, S. Brunner, L. Villard, B. F. McMillan, S. Jolliet, T. M. Tran, A. Bottino, and J. P. Graves, *Phys Plasmas* **17**, 122301 (2010)
[58] P. Helander, *Plasma Phys. Control. Fusion* **37**, 57 (1995)